Editors' Suggestion | Featured in Physics

Pauli Blockade of Tunable Two-Electron Spin and Valley States in Graphene Quantum Dots

Chuyao Tong,[1,*] Annika Kurzmann,[1] Rebekka Garreis,[1] Wei Wister Huang,[1] Samuel Jele,[1] Marius Eich,[1] Lev Ginzburg,[1] Christopher Mittag,[1] Kenji Watanabe,[2] Takashi Taniguchi,[3] Klaus Ensslin,[1] and Thomas Ihn[1]

[1]*Solid State Physics Laboratory, ETH Zurich, CH-8093 Zurich, Switzerland*

[2]*Research Center for Functional Materials, National Institute for Materials Science, 1-1 Namiki, Tsukuba 305-0044, Japan*

[3]*International Center for Materials Nanoarchitectonics, National Institute for Materials Science, 1-1 Namiki, Tsukuba 305-0044, Japan*

(Received 23 July 2021; revised 23 November 2021; accepted 10 January 2022; published 9 February 2022)

Pauli blockade mechanisms—whereby carrier transport through quantum dots (QD) is blocked due to selection rules even when energetically allowed—are a direct manifestation of the Pauli exclusion principle, as well as a key mechanism for manipulating and reading out spin qubits. The Pauli spin blockade is well established for systems such as GaAs QDs, but is to be further explored for systems with additional degrees of freedom, such as the valley quantum numbers in carbon-based materials or silicon. Here we report experiments on coupled bilayer graphene double quantum dots, in which the spin and valley states are precisely controlled, enabling the observation of the two-electron combined blockade physics. We demonstrate that the doubly occupied single dot switches between two different ground states with gate and magnetic-field tuning, allowing for the switching of selection rules: with a spin-triplet–valley-singlet ground state, valley blockade is observed; and with the spin-singlet–valley-triplet ground state, robust spin blockade is shown.

DOI: 10.1103/PhysRevLett.128.067702

Graphene quantum dots (QDs) have been proposed to host spin qubits with long spin coherence times [1,2], especially promising in bilayer graphene (BLG) due to its smaller spin-orbit coupling compared with that of carbon nanotubes [3–7]. In BLG, a band gap can be opened by an electric field perpendicular to the BLG sheet [8–10]. Together with recent advancements in fabrication technology [11], the quality of state-of-the-art BLG QDs has been raised to such a level that highly tunable QDs [6,7,12–17] can now be fabricated.

Observation of the Pauli blockade is a crucial step toward qubit manipulation and read out. A coupled double QD occupied by two carriers can be tuned to a regime where two states coexist: one carrier on each dot, or both carriers on the same dot. Transitions between these states can be blocked by selection rules based on the Pauli exclusion principle. Observation of a two-electron Pauli spin blockade relies on the single-dot two-electron spin-singlet and -triplet states to be well separated in energy, with the spin singlet being the ground state (GS). This usually arises naturally at zero magnetic field [4,5,18–20]. In BLG QDs however, at low magnetic field, the single-dot two-carrier GS is observed to be a spin triplet [14,15,21] due to the additional valley degrees of freedom $K^{-/+}$.

Unlike the low-lying valleys in silicon, complicating qubit control by providing additional coherence channels [22–24], energy splittings of BLG valley states are reliably tunable by perpendicular magnetic fields [12–15] and by gate voltages [13,25], and are themselves good quantum numbers. Selection rules involving valleys have been seen in carbon nanotubes and silicon [4,5,26], although with limited control. In our coupled double QDs, valley tunability allows us to study the combined spin and valley blockade physics, demonstrating controlled switching between a spin-triplet–valley-singlet at low, and spin-singlet–valley-triplet single-dot two-electron state at high magnetic field. In this way, we show canonical two-electron blockade physics by performing finite-bias measurements, and observe valley blockade in the former and spin blockade in the latter regime.

We utilized the tunable BLG band gap [8–10] to form a coupled electron double QD with n-type leads [Fig. 1(a), see Supplemental Material, Sec. S1 [27]]. Barrier-gate (green) voltages $V_{\mathrm{LB,MB,RB}}$ provide individual control of the dot-lead [13,28], and interdot tunnel coupling [17]. Dots L, R are independently controlled by the plunger-gate (yellow) voltages $V_{L,R}$. A bias-voltage V_{SD} is applied symmetrically between the source $(+V_{\mathrm{SD}}/2)$ and drain $(-V_{\mathrm{SD}}/2)$, and the current is measured.

The charge-stability map [Fig. 1(b)] displays honeycomb patterns. Regions of low conductance suppressed by Coulomb-blockade are labeled (N_L, N_R), with stable electron numbers in the left (N_L) and in the right (N_R) dot. Transport resumes at intersections of Coulomb resonances

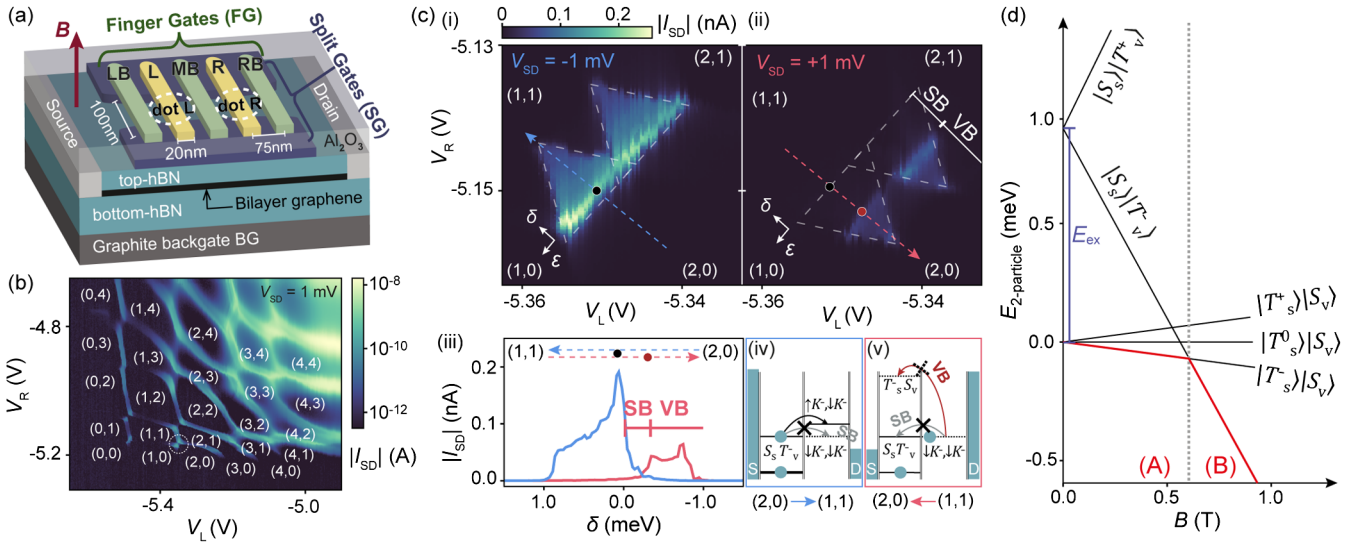

FIG. 1. (a) Device illustration. Double electron dots are defined with plunger gates L and R, and barrier gates LB, MB, and RB. A magnetic field B is applied perpendicular to the BLG. (b) Charge-stability diagram at $V_{B_M} = -5.76$ V. (c) Finite-bias triangles at $V_{\mathrm{MB}} = -5.76$ V, $B = 800$ mT with (i) negative and (ii) positive source-drain bias V_{SD}. ϵ is the total energy, and detuning $\delta = \epsilon_L - \epsilon_R$ the interdot energy difference. (iii) Line cuts along the dashed arrows, with $V_{L,R}$ converted into δ. $\delta = 0$ at the baseline of bias triangles. Current peaks are labeled by dots. Valley blockade (VB) and spin blockade (SB) suppress current in the positive-bias direction. Energies of relevant states are sketched for $\delta = 0$ in (iv) and (v). For negative bias [electron transport $(2,0) \rightarrow (1,1)$], the spin-blockaded GS–GS transition [gray in (iv)] is readily circumvented by a transition close in energy (black). For positive bias [electron transport $(1,1) \rightarrow (2,0)$], the next available transition is higher in energy [red in (v)] and requires a valley flip. (d) Evolution of single-dot two-particle energies in magnetic field, sketched with $E_{\mathrm{ex}} = 0.9$ eV, $g_v = 28$, and $g_s = 2$. The two different GSs (red) define regime A and B.

of the two dots, and pairs of triple points of high conductance appear. Three double dot charge occupancies coexist at the triple point that they are adjacent to, and allow for charge transport via these three states. More negative plunger-gate voltages $V_{L,R}$ deplete the respective dots down to the last electron.

A finite bias voltage V_{SD} expands triple points into finite-bias triangles, whose orientation depends on the sign of V_{SD}. Within the bias triangles, energies of the relevant states are tuned into the bias window, such that these states are accessible and allow for charge transport. We look at the two-electron transport at the triple points encircled in Fig. 1(b), where transitions between the two-electron charge occupation (1, 1) (one electron on each dot) and (2, 0) (both electrons on the left dot) states govern the transport. [Note that we observe the same physics around the charge occupation (1, 1) and (0, 2), only swapping the role of the left and the right dot; see Supplemental Material, Sec. S6 [27]]. An example of a current map of bias triangles at $B = 800$ mT is shown in Fig. 1(c). In one bias direction [Fig. 1(c,i)], the high conductance bias triangles are complete; in the other bias direction [Fig. 1(c,ii)] however, the triangles appear smaller with a missing baseline. Here, energetically allowed transitions are blocked by the Pauli exclusion principle, blocking charge transport and suppressing current, demonstrating the Pauli blockade effect. Comparing line cuts [Fig. 1(c,iii)] along the dashed arrows we see the following: At the baselines (black dots), for negative bias the peak current is ~180 pA, whereas for positive bias it is masked by the noise floor (~300 fA). In the remaining part of the positive-bias triangles, the current is ~3 times weaker compared with that in the negative-bias ones. In the following discussion, and with the aid of schematics [Figs. 1(c,iv) and 1(c,v)], we will attribute the missing baseline to spin blockade, and the weaker current in the tip of the triangle to valley blockade.

A thorough understanding of the relevant (1, 1) and (2, 0) states is crucial for interpreting the nature of the blockade. Here, we introduce the recently established level spectrum of one- and two-particle states in single BLG QDs [6,7,13–16,31,32], and limit our discussion to the lowest orbital state (the next orbital state is > 1.7 meV higher in energy; see Supplemental Material, Secs. S2 and S3 [27]).

Within the first energy shell, the single-dot–single-particle states are fourfold degenerate. A small spin-orbit coupling $\Delta_{\mathrm{SO}} \sim 80$ μeV [6,7] splits them into two Kramer pairs, $|\downarrow K^-\rangle$ and $|\uparrow K^+\rangle$, and $|\uparrow K^-\rangle$ and $|\downarrow K^+\rangle$ (see Supplemental Materials, Sec. S1 [27]). A magnetic field splits the spin states by $\Delta E_{\uparrow/\downarrow} = \pm g_s \mu_B B/2$ in energy, where $g_s = 2$ [12,14,15]. Analogously, the valleys $K^\pm$ couple to a perpendicular magnetic field with $\Delta E_{K^\pm} = \pm g_v \mu_B B_\perp/2$, linearly in the low-field limit. The valley g factor g_v is an order of magnitude larger than the spin g factor g_s [12,13,15].

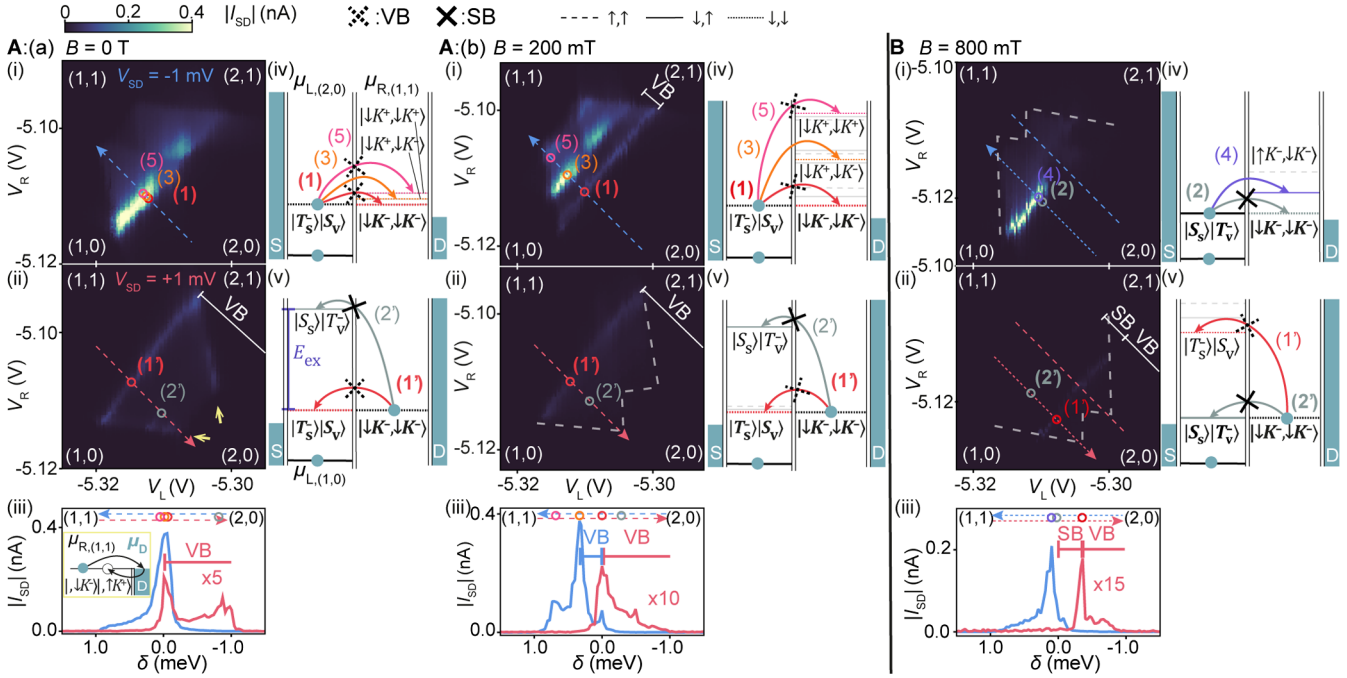

FIG. 2. Finite-bias triangles at $V_{\mathrm{MB}} = -5.81$ V in **A**: regime A with $(2,0)_{\mathrm{GS}}$: $|T_s^-\rangle|S_v\rangle$ at $B =$ (*a*) 0 T and (b) 200 mT, and in **B**: regime B with $(2,0)_{\mathrm{GS}}$: $|S_s\rangle|T_v^-\rangle$ at $B = 800$ mT for (i) negative [electron transport $(2,0) \to (1,1)$], and (ii) positive [electron transport $(1,1) \to (2,0)$] source-drain bias V_{SD}. (iv), (v) Schematics of electrochemical potentials μ of relevant transitions for (i), (ii), sketched at $\delta = 0$, when μ_{GS}s align. Nonzero δ allows for higher energy transitions. (iii) Line cuts along the dashed arrow, with $V_{L,R}$ converted into δ. Current resonances are labeled by numbered colored circles. Valley-blockade (VB) and spin-blockade (SB) regions are marked. Current is suppressed for positive bias $(1,1) \to (2,0)$ by the valley and spin blockade, and is enhanced for clarity in the line cuts (iii) by a factor of 5, 10, and 15 for A(a), A(b), and B. In A(a,ii), the valley blockade is lifted at the edges of the triangles, where the electron in the dot can exchange with electrons in the source or drain leads [yellow arrows in A(a,ii) and schematic outlined in yellow in A(a,iii)]. In B, the line cut is taken at the dotted instead of the dashed line, due to a shift of the bias triangle along the ϵ direction, a result of the change of $(2,0)_{\mathrm{GS}}$.

For weakly coupled double dots, exchange interaction is negligible between two electrons, each residing on one dot. The (1, 1) basis states can therefore be approximated as product states of two sets of single-dot–single-particle states, generating 16 (1, 1) basis states with ten distinct energies $E_{(1,1)}$ that are sums of the energies of the two sets (shown in Supplemental Material, Sec. S4 [27]). The ground state $(1,1)_{\mathrm{GS}}$ is always $|\downarrow K^-, \downarrow K^-\rangle$.

Contrarily, the (2, 0) states are better described in the basis of spin and valley singlet and triplets. We consider only the lower symmetric orbital wave function, so that the product of the valley and spin states is necessarily antisymmetric. In this way, we reduce the 16 basis states to six. Evolution of this single-dot two-particle spectrum [15,31,32] in a perpendicular magnetic field is sketched in Fig. 1(d). At low field, the spin-triplet–valley-singlet states $|T_s^{-/0/+}\rangle|S_v\rangle$ are lower in energy than the spin-singlet–valley-triplets, $|S_s\rangle|T_v^{-/+}\rangle$, by the exchange energy E_{ex}. At high field, $|S_s\rangle|T_v^-\rangle$ is lowered enough in energy due to coupling with the magnetic field to become the GS. We therefore separate the discussion into two regimes, where the $(2,0)_{\mathrm{GS}}$ is $|T_s^-\rangle|S_v\rangle$ in regime A, and $|S_s\rangle|T_v^-\rangle$ in regime B.

With the knowledge of the expected (1, 1) and (2, 0) states, we look in Fig. 2 at finite-bias triangles with low interdot coupling, where occurrences of elastic tunnelings are observed as current resonances in the left and right dot energy difference, i.e., the detuning axis $\delta = \epsilon_L - \epsilon_R$. The different appearances of the three pair of triangles indicate distinct sets of transitions involved, but the current at positive bias is always suppressed compared with negative bias: Unless higher orbital states are within reach in the bias window, due to the Pauli exclusion principle, there exist no (2, 0) states matching both spin and valley quantum numbers of the $(1,1)_{\mathrm{GS}}$ $|\downarrow K^-, \downarrow K^-\rangle$.

In regime A (Fig. 2A), states involved in the GS-GS transitions $(1), (1')$ (red) have mismatching valleys. Unless another transition channel from the GSs exists, allowing the electron to bypass this blockade, an electron loaded into the GSs would be stuck and would suppress the current at the baselines, until a valley-flip event occurs.

However, at $B = 0$ T the baseline for $(2,0) \to (1,1)$ [Fig. 2A(a,i)] is strong, with a peak current of ~350 pA [Fig. 2A(a,iii)], as the valley-blockaded transition (1) (red) is easily circumvented by the nonblockaded transition (3) (orange), because the (1, 1) states $|\downarrow K^-, \downarrow K^-\rangle$ and

$|\downarrow K^-, \downarrow K^+\rangle$ (or $|\downarrow K^+, \downarrow K^-\rangle$) are nearly degenerate in energy at $B = 0$ T. At $B = 200$ mT [Fig. 2A(b)], these (1, 1) states are valley split in energy by $g_v \mu_B B$. Hence, transitions (1) and (3) no longer occur at the same energy, as (1) is lowered in detuning while (3) stayed the same. We see therefore in Fig. 2A(b,i) a valley-blockaded region with suppressed current, which at higher δ is lifted by the onset of transition (3).

By contrast, for $(1,1) \rightarrow (2,0)$ [Figs. 2A(a,ii) and 2A(b,ii)] the valley blockade cannot be circumvented by another transition. Current at the baseline is suppressed by a factor larger than 5 at $B = 0$ T, and larger than 10 at $B = 200$ mT. This is because the next available (2, 0) state accessible from the $(1,1)_{\mathrm{GS}}$: $|\downarrow K^-, \downarrow K^-\rangle$ with matching valleys is $|S_s\rangle|T_v^-\rangle$. Transition $(2')$ (gray) to this state is not only higher in energy, but also requires a spin flip. Even at finite δ where enough energy is provided, no lifting of the valley blockade via this spin-mismatched transition is observed.

The valley blockade is lifted at $B = 0$ T at the outer edges of the triangles [Fig. 2A(a,ii), yellow arrows], with current similar to the nonblockaded inelastic current. At the edges, the GS electrochemical potential of the right dot $\mu_{R,(1,1)\mathrm{GS}}$ is aligned with the drain μ_D [2,20,33], allowing an electron with blockaded quantum numbers to tunnel back into the lead, in exchange for one with quantum numbers that allow the transport to continue. This lifting is no longer observed at finite field $B = 200$ mT in Fig. 2A(b,ii), as the blockaded $(1,1)_{\mathrm{GS}}$ $|\downarrow K^-, \downarrow K^-\rangle$ and the nonblockaded (1, 1) state $|\downarrow K^-, \downarrow K^+\rangle$ are split by $g_v \mu_B B$, more than the thermal energy.

In regime B at a higher field, when $(2,0)_{\mathrm{GS}}$ becomes $|S_s\rangle|T_v^-\rangle$ (Fig. 2B), the GS-GS transitions (2) and $(2')$ are spin blockaded. However, for the $(2,0) \rightarrow (1,1)$ bias direction [Fig. 2B(i)], the spin-blockaded transition (2) (gray) can be circumvented via transition (4) (purple) that is very close in energy (only a Zeeman splitting higher in detuning; see Supplemental Material, Sec. S5, for more details), with a peak current of 200 pA [Fig. 2B(iii)].

For $(1,1) \rightarrow (2,0)$ [Fig. 2B(ii)], the spin-blockade leakage current is smaller than the noise floor. The next available transition in detuning is the valley-blockaded transition $(1')$ (red) discussed above. This transition is observed at larger δ, with a peak current of 10 pA. Spin conservation during interdot tunneling is a stronger condition than valley conservation, as the valley blockaded transition $(1')$ lifts the spin blockade [Fig. 2B(ii)], but the spin-blockaded transition $(2')$ cannot lift the valley blockade [Fig. 2A(a,ii)]. When increasing interdot coupling, we enhance current from transport via nonelastic tunneling, and arrive at the Fig. 1(c) shown before.

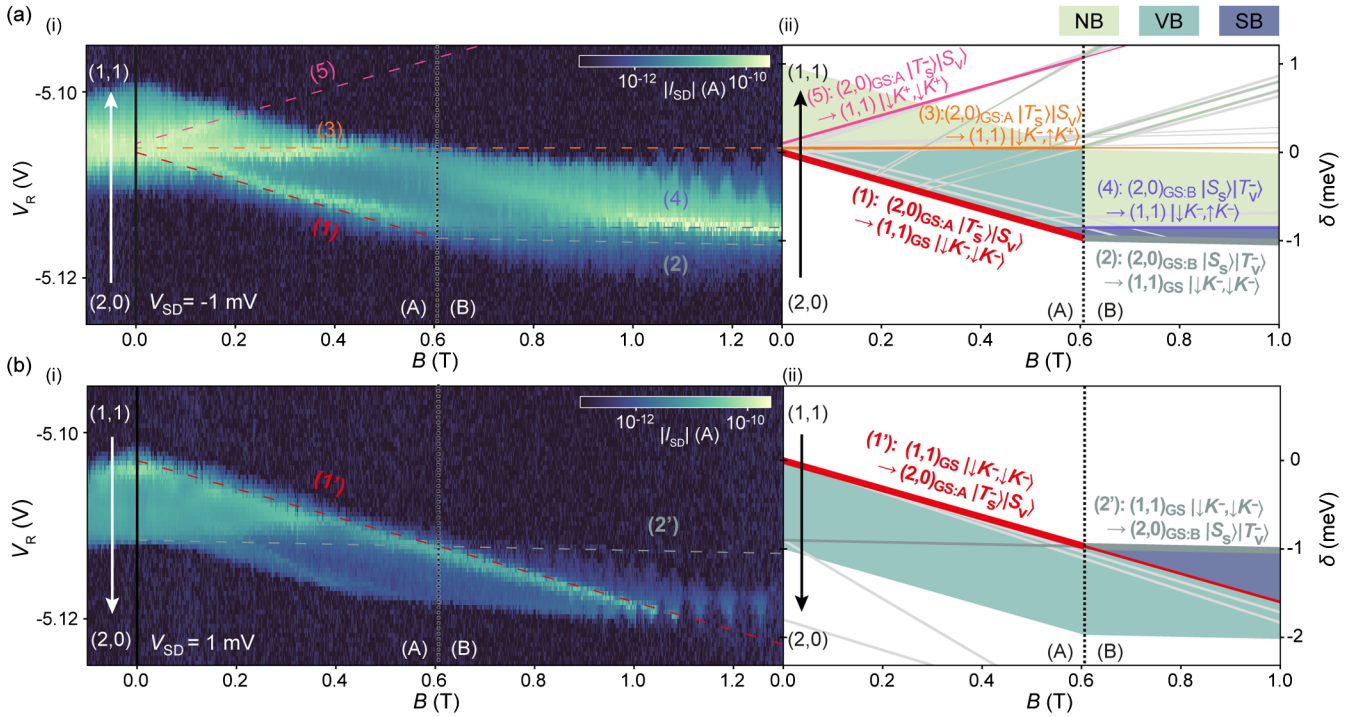

FIG. 3. Evolution in magnetic field of GS transitions for (a) negative and (b) positive source-drain bias V_{SD}. Evolution in magnetic field for (i) line cut along the δ axis (dashed arrows in Fig. 2A) and (ii) calculated transitions with $E_{\mathrm{ex}} = 0.9$ meV, $\Delta_{\mathrm{SO}} = 80$ μeV, $g_v = 28$, and $g_s = 2$, from $(2,0)_{\mathrm{GS}}$ in (a,ii), and from $(1,1)_{\mathrm{GS}}$ in (b,ii). Except for the GS-GS transition (2) and $(2')$, transitions requiring spin flips [sketched in light gray in (ii)] are not labeled. The thicker lines in (ii) represent the GS-GS transitions, and hence define the baselines of the bias triangles. Yellow, blue, and purple represent nonblockaded (NB), VB, and SB regions, respectively. At high field, oscillations periodic in $1/B$ are observed for both bias directions [29].

We inspect the line cuts along the δ axis (dashed arrows in Fig. 2A) in the magnetic field for the continuous evolution of the identified transitions. The results are displayed in Figs. 3(a,i) and 3(b,i) for $(2,0) \rightarrow (1,1)$ and $(1,1) \rightarrow (2,0)$, respectively. The corresponding calculated transition energies are plotted in Figs. 3(a,ii) and 3(b,ii) (see Supplemental Material, Sec. S4 for evolution of the states). V_{SD} opens up a bias window of 1 meV starting from the baseline, shown as higher conductance regions in the measurements (a,i) and (b,i), and colored regions in the calculated transitions (a,ii) and (b,ii). Beyond the bias window, electron occupancy is Coulomb blockaded in either (1, 1) or (2, 0).

For $(2,0) \rightarrow (1,1)$, in regime A, transitions (1), (3), and (5) split linearly in energy with the magnetic field, with $g_v \approx 28$, corresponding to the (1, 1) valley configurations $|K^-, K^-\rangle$, $|K^-, K^+\rangle$, $(|K^+, K^-\rangle)$, and $|K^+, K^+\rangle$. The kink in the baseline [red and gray in Fig. 3(a)] indicates the change of GS-GS transitions from (1) to (2), caused by the change of the $(2,0)_{\mathrm{GS}}$ from $|T_s^-\rangle|S_v\rangle$ to $|S_s\rangle|T_v^-\rangle$.

For $(1,1) \rightarrow (2,0)$, only the valley-blockaded transition $(1')$ is observed. At high field, the bias window diminishes and the edges appear no longer parallel to $(1')$, but to $(2')$ instead. This indicates the change of the GS-GS transition from $(1')$ [red in Fig. 3(b)] to the spin-blockaded transition $(2')$ (gray), with resonance masked by the noise floor.

Regions of no blockade, valley blockade, and spin blockade are labeled in Figs. 3(a,ii) and 3(b,ii). Current strength in these regions decreases due to the blockade effect in this order [Figs. 3(a,i) and 3(b,i)]. The singlet-triplet energy splitting, crucial for spin-qubit operation, can be tuned in magnitude by magnetic field, or by tuning the valley g factor with gate voltages [13].

In conclusion, in our BLG QDs we show controlled switching between two regimes: At low perpendicular magnetic field, the (2, 0) ground state is a spin-triplet valley-singlet, allowing for the observation of valley blockade, whereas at higher field, the spin-singlet valley-triplet (2, 0) ground state allows for the observation of a robust spin blockade. These results demonstrate exquisite control over spin and valley states, a thorough understanding of the intricate two-particle Hilbert space, and high sample quality of our BLG QDs. The observation of the blockade paves the way for future graphene-based spin and valley qubits.

The supporting data for this Letter are openly available from Ref. [34].

The authors declare no competing interests.

We thank P. Märki and T. Bähler as well as the FIRST staff for their technical support. We acknowledge funding from the Core3 European Graphene Flagship Project, the Swiss National Science Foundation via NCCR Quantum Science and Technology, and the EU Spin-Nano RTN network. R. G. acknowledges funding from the European Union's Horizon 2020 research and innovation programme under the Marie Skłodowska-Curie Grant Agreement No. 766025. Growth of hexagonal boron nitride crystals was supported by the elemental Strategy Initiative conducted by the MEXT, Japan and JSPS KAKENHI Grant No. JP15K21722.

*ctong@phys.ethz.ch

[1] B. Trauzettel, D. V. Bulaev, D. Loss, and G. Burkard, Spin qubits in graphene quantum dots, Nat. Phys. **3**, 192 (2007).
[2] R. Hanson, L. P. Kouwenhoven, J. R. Petta, S. Tarucha, and L. M. K. Vandersypen, Spins in few-electron quantum dots, Rev. Mod. Phys. **79**, 1217 (2007).
[3] F. Pei, E. A. Laird, G. A. Steele, and L. P. Kouwenhoven, Valley–spin blockade and spin resonance in carbon nanotubes, Nat. Nanotechnol. **7**, 630 (2012).
[4] H. O. H. Churchill, A. J. Bestwick, J. W. Harlow, F. Kuemmeth, D. Marcos, C. H. Stwertka, S. K. Watson, and C. M. Marcus, Electron–nuclear interaction in 13 c nanotube double quantum dots, Nat. Phys. **5**, 321 (2009).
[5] M. R. Buitelaar, J. Fransson, A. L. Cantone, C. G. Smith, D. Anderson, G. A. C. Jones, A. Ardavan, A. N. Khlobystov, A. A. R. Watt, K. Porfyrakis, and G. A. D. Briggs, Pauli spin blockade in carbon nanotube double quantum dots, Phys. Rev. B **77**, 245439 (2008).
[6] A. Kurzmann, Y. Kleeorin, C. Tong, R. Garreis, A. Knothe, M. Eich, C. Mittag, C. Gold, F. K. de Vries, K. Watanabe, T. Taniguchi, V. Fal'ko, Y. Meir, T. Ihn, and K. Ensslin, Kondo effect and spin-orbit coupling in graphene quantum dots, Nat. Commun. **12**, 6004 (2021).
[7] L. Banszerus, S. Möller, C. Steiner, E. Icking, S. Trellenkamp, F. Lentz, K. Watanabe, T. Taniguchi, C. Volk, and C. Stampfer, Spin-valley coupling in single-electron bilayer graphene quantum dots, Nat. Commun. **12**, 5250 (2021).
[8] T. Ohta, A. Bostwick, T. Seyller, K. Horn, and E. Rotenberg, Controlling the electronic structure of bilayer graphene, Science **313**, 951 (2006).
[9] E. McCann, Asymmetry gap in the electronic band structure of bilayer graphene, Phys. Rev. B **74**, 161403(R) (2006).
[10] J. B. Oostinga, H. B. Heersche, X. Liu, A. F. Morpurgo, and L. M. Vandersypen, Gate-induced insulating state in bilayer graphene devices, Nat. Mater. **7**, 151157 (2008).
[11] H. Overweg, H. Eggimann, X. Chen, S. Slizovskiy, M. Eich, R. Pisoni, Y. Lee, P. Rickhaus, K. Watanabe, T. Taniguchi *et al.*, Electrostatically induced quantum point contacts in bilayer graphene, Nano Lett. **18**, 553 (2018).
[12] M. Eich, F. Herman, R. Pisoni, H. Overweg, A. Kurzmann, Y. Lee, P. Rickhaus, K. Watanabe, T. Taniguchi, M. Sigrist, T. Ihn, and K. Ensslin, Spin and Valley States in Gate-Defined Bilayer Graphene Quantum Dots, Phys. Rev. X **8**, 031023 (2018).
[13] C. Tong, R. Garreis, A. Knothe, M. Eich, A. Sacchi, K. Watanabe, T. Taniguchi, V. Fal'ko, T. Ihn, K. Ensslin, and A. Kurzmann, Tunable valley splitting and bipolar operation in graphene quantum dots, Nano Lett. **21**, 1068 (2021).
[14] R. Garreis, A. Knothe, C. Tong, M. Eich, C. Gold, K. Watanabe, T. Taniguchi, V. Fal'ko, T. Ihn, K. Ensslin, and A. Kurzmann, Shell Filling and Trigonal Warping in

Graphene Quantum Dots, Phys. Rev. Lett. **126**, 147703 (2021).

[15] A. Kurzmann, M. Eich, H. Overweg, M. Mangold, F. Herman, P. Rickhaus, R. Pisoni, Y. Lee, R. Garreis, C. Tong, K. Watanabe, T. Taniguchi, K. Ensslin, and T. Ihn, Excited States in Bilayer Graphene Quantum Dots, Phys. Rev. Lett. **123**, 026803 (2019).

[16] L. Banszerus, A. Rothstein, T. Fabian, S. Möller, E. Icking, S. Trellenkamp, F. Lentz, D. Neumaier, K. Watanabe, T. Taniguchi *et al.*, Electron–hole crossover in gate-controlled bilayer graphene quantum dots, Nano Lett. **20**, 7709 (2020).

[17] L. Banszerus, A. Rothstein, E. Icking, S. Möller, K. Watanabe, T. Taniguchi, C. Stampfer, and C. Volk, Tunable interdot coupling in few-electron bilayer graphene double quantum dots, Appl. Phys. Lett. **118**, 103101 (2021).

[18] K. Ono, D. Austing, Y. Tokura, and S. Tarucha, Current rectification by Pauli exclusion in a weakly coupled double quantum dot system, Science **297**, 1313 (2002).

[19] J. R. Petta, A. C. Johnson, J. M. Taylor, E. A. Laird, A. Yacoby, M. D. Lukin, C. M. Marcus, M. P. Hanson, and A. C. Gossard, Coherent manipulation of coupled electron spins in semiconductor quantum dots, Science **309**, 2180 (2005).

[20] A. C. Johnson, J. R. Petta, C. M. Marcus, M. P. Hanson, and A. C. Gossard, Singlet-triplet spin blockade and charge sensing in a few-electron double quantum dot, Phys. Rev. B **72**, 165308 (2005).

[21] S. Möller, L. Banszerus, A. Knothe, C. Steiner, E. Icking, S. Trellenkamp, F. Lentz, K. Watanabe, T. Taniguchi, L. Glazman, V. Fal'ko, C. Volk, and C. Stampfer, Probing Two-Electron Multiplets in Bilayer Graphene Quantum Dots, Phys. Rev. Lett. **127**, 256802 (2021).

[22] F. A. Zwanenburg, A. S. Dzurak, A. Morello, M. Y. Simmons, L. C. L. Hollenberg, G. Klimeck, S. Rogge, S. N. Coppersmith, and M. A. Eriksson, Silicon quantum electronics, Rev. Mod. Phys. **85**, 961 (2013).

[23] B. M. Maune, M. G. Borselli, B. Huang, T. D. Ladd, P. W. Deelman, K. S. Holabird, A. A. Kiselev, I. Alvarado-Rodriguez, R. S. Ross, A. E. Schmitz *et al.*, Coherent singlet-triplet oscillations in a silicon-based double quantum dot, Nature (London) **481**, 344 (2012).

[24] E. Kawakami, P. Scarlino, D. R. Ward, F. Braakman, D. Savage, M. Lagally, M. Friesen, S. N. Coppersmith, M. A. Eriksson, and L. Vandersypen, Electrical control of a long-lived spin qubit in a Si/SiGe quantum dot, Nat. Nanotechnol. **9**, 666 (2014).

[25] H. Chen, P. Zhou, J. Liu, J. Qiao, B. Oezyilmaz, and J. Martin, Gate controlled valley polarizer in bilayer graphene, Nat. Commun. **11**, 1 (2020).

[26] J. K. Perron, M. J. Gullans, J. M. Taylor, M. D. Stewart, and N. M. Zimmerman, Valley blockade in a silicon double quantum dot, Phys. Rev. B **96**, 205302 (2017).

[27] See Supplemental Materials at http://link.aps.org/supplemental/10.1103/PhysRevLett.128.067702 for discussions on the sample and fabrication methods, the one-electron bias triangles, a list of energy states and relevant transitions, and data on the mirrored charge occupation $(1,1) \leftrightarrow (0,2)$ which includes Refs. [6,13,15,17,28–30].

[28] M. Eich, R. Pisoni, A. Pally, H. Overweg, A. Kurzmann, Y. Lee, P. Rickhaus, K. Watanabe, T. Taniguchi, K. Ensslin, and T. Ihn, Coupled quantum dots in bilayer graphene, Nano Lett. **18**, 5042 (2018).

[29] L. Banszerus, T. Fabian, S. Möller, E. Icking, H. Heiming, S. Trellenkamp, F. Lentz, D. Neumaier, M. Otto, K. Watanabe *et al.*, Electrostatic detection of Shubnikov–de Haas oscillations in bilayer graphene by coulomb resonances in gate-defined quantum dots, Phys. Status Solidi B **257**, 2000333 (2020).

[30] L. Wang, I. Meric, P. Huang, Q. Gao, Y. Gao, H. Tran, T. Taniguchi, K. Watanabe, L. Campos, D. Muller *et al.*, One-dimensional electrical contact to a two-dimensional material, Science **342**, 614 (2013).

[31] A. Knothe and V. Fal'ko, Quartet states in two-electron quantum dots in bilayer graphene, Phys. Rev. B **101**, 235423 (2020).

[32] A. Knothe, L. I. Glazman, and V. I. Fal'ko, Theory of tunneling spectra for a few-electron bilayer graphene quantum dot, arXiv:2104.03399.

[33] T. Ihn, *Semiconductor Nanostructures: Quantum States and Electronic Transport* (Oxford University Press, New York, 2010).

[34] C. Tong, A. Kurzmann, R. Garreis, W. W. Huang, S. Jele, M. Eich, L. Ginzburg, C. Mittag, K. Watanabe, T. Taniguchi, K. Ensslin, and T. Ihn, Data repository: Pauli blockade of tunable two-electron spin and valley states in graphene quantum dots (2022), 10.3929/ethz-b-000528896.